Bull. Mater. Sci. (2021) 44:109
https://doi.org/10.1007/s12034-021-02368-8

Effects of sonication power on electrochemical performance of ZrO_2-decorated $LiMn_2O_4$ cathode material for LIBs

MEHMET EMRE CETINTASOGLU[1] and OZGUL KELES[2,*]

[1]Department of Chemical Oceanography, Institute of Marine Sciences and Management, Istanbul University, Istanbul 34134, Turkey

[2]Department of Metallurgical and Materials Engineering, Istanbul Technical University, Istanbul 34469, Turkey

*Author for correspondence (ozgulkeles@itu.edu.tr)

MS received 14 July 2020; accepted 31 October 2020

Abstract. The $LiMn_2O_4$ (LMO) powder is decorated with ZrO_2 (denoted as Zr@LMO) particles by using sonication-assisted sol–gel method. Different sonication powers (10, 30 and 50%) are used to disperse ZrO_2 and the effects of ZrO_2 distribution at $LiMn_2O_4$'s electrochemical performance are analysed. Scanning electron microscopy and energy dispersive spectroscopy analyses have been made on laminated samples. For the structural analyses of particles, X-ray diffractometer is used. Electrochemical performances of electrodes are tested with galvanostatic measurements, cyclic voltammograms and electrochemical impedance spectroscopy. The ZrO_2 distribution ratio on the particle surfaces is improved by 10% with the increase of sonication power from 10 to 50%. Therefore, at 50% sonication power, lower charge transfer resistance and side reactions (Mn dissolution) are accomplished, which leads to 41 and 9% specific capacity increase compared to pure and the lowest sonication power, respectively. After 100 cycles at 0.1C, 93.2 mAh g^{-1} specific discharge capacity and 73.4% capacity retention are attained for ZrO_2-decorated LMO at 50% sonication power. Furthermore, at 2C rate, the specific discharge capacity of the decorated sample at 50% sonication power is 59% higher than the pure LMO.

Keywords. $LiMn_2O_4$ cathode; lithium-ion battery; ultrasonic sonication; sol–gel; surface decoration.

1. Introduction

Each day, consumer requirements are pushing the limits of advanced energy storage devices. The main requirements are high energy density, long-lasting, easy maintainability, environmentally benign, short charge time, and safety [1]. Therefore, great efforts have made to commercialize new active materials and to improve the cyclic performance of existing active materials [2–7].

$LiMn_2O_4$ is one of the most promising candidates among other metal oxides due to its high working voltage (~4.0 V *vs.* Li/Li^+), low toxicity and low cost. Having a three-dimensional spinel structure also improves the rate capability of electrodes due to the high Li-ion diffusion rate. However, spinel structures limit the cycle life of $LiMn_xO_y$-based electrodes [8]. One of the main drawbacks of $LiMn_2O_4$ is the dissolution of Mn due to the possible reactions of lithium hexafluorophosphate ($LiPF_6$) with a water residue inside the cell, leading to the formation of HF. Therefore, subduing Mn dissolution from the $LiMn_2O_4$ is a crucial factor to reduce capacity fading [9].

Several methods have been developed to reduce the Mn dissolution. One of them is cationic doping in order to increase the stability of the $LiMn_2O_4$ crystal structure by replacing Mn with cations such as Ti^{4+} or Al^{3+} [10]. However, the downside of this approach is that these dopant ions are electrochemically inactive and lead to a specific capacity loss for active materials. In order to improve both capacity and cycling performance, Co^{2+} or Ni^{2+} can be used as dopant ions but the chemical activity of $LiMn_2O_4$ increases with such dopants, especially Ni^{+4} and this leads to safety problems in $LiMn_2O_4$ cells [11]. Another approach is using conductive carbon as a coating material. Although electrochemical performance is improved with a carbon coating, it has strong reducibility on Mn-ion; thus, it is hard to apply it to $LiMn_2O_4$ [12].

Surface modification [13,14] is an important technique to enhance the cyclic performances of cathode active materials, as the cathode electrolyte interface is far thinner than the solid electrolyte interface (SEI) of anodes. Thus, there should be an extra passivation film at the surface of cathodes in order to prevent the irreversible side reactions that cause the loss of active material [15]. Different types of oxides, fluorides and polymers are used to protect the cathode surface from highly reactive HF [16–21].

ZrO_2 has excellent corrosive resistance against reactive compounds due to its high chemical stability [22–24]. Thus, ZrO_2 has been examined as a surface modifier to reduce interaction with undesired compounds that occurred in electrolytes and improve the cyclability of cathode active

Published online: 22 April 2021

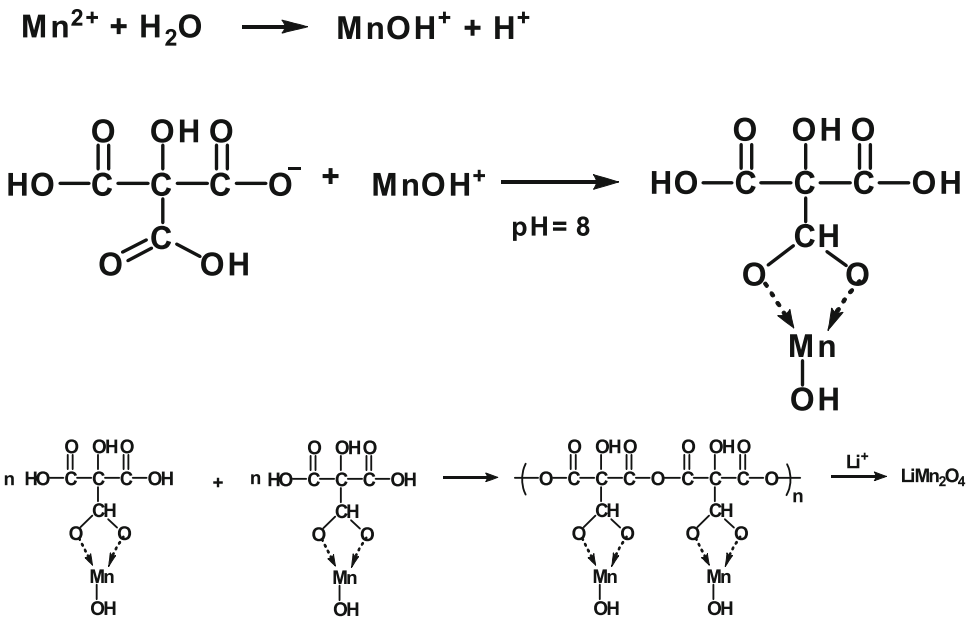

Figure 1. Possible chemical reactions of $LiMn_2O_4$ synthesis via sol–gel method.

materials, such as $LiNi_{0.6}Co_{0.2}Mn_{0.2}O_2$ [25], $Li[Li_{0.2}Mn_{0.54}Ni_{0.13}Co_{0.13}]O_2$ [26] $LiNi_{1/3}Mn_{1/3}Co_{1/3}O_2$ [27], $LiCoO_2$ [28] and $Li_3V_2(PO_4)_3$ [22]. In these studies, the ZrO_2 decoration has been done by stirring or sonication processes but there is no detail on the effects of the process parameters. Therefore, a hypothesis was built on this study to investigate the distribution of ZrO_2 particles over the $LiMn_2O_4$ surface by using different sonication powers. Various sonication powers have been tried during the gelation of ZrO_2 over $LiMn_2O_4$ and their electrochemical performance has been examined.

2. Experimental

2.1 *Materials synthesis*

2.1a *Synthesis of $LiMn_2O_4$*: $LiMn_2O_4$ powder is synthesized by a sol–gel route. Li acetate dihydrate ($CH_3COOLi{\cdot}2H_2O$), Mn acetate tetrahydrate ($(CH_3COO)_2Mn{\cdot}4H_2O$) and citric acid are dissolved in distilled water with the Mn:Li:citric acid (2:1:3) stoichiometry. The solution pH is set to 9 by adding ammonia. The obtained gel is dried at 100°C for 24 h and then a two-step heat treatment is applied. First, to remove organic compounds, the attained gel is exposed to 500°C for 5 h. Then, the powders are subjected to 750°C for 10 h for crystallization. The possible chemical reactions are shown in figure 1.

2.1b *Preparation of ZrO_2-decorated $LiMn_2O_4$ electrode*: The surface decoration is performed by adding $LiMn_2O_4$ powders into a zirconia sol, as shown in figure 2. The preparation of ZrO_2 sol is started by diluting 70 wt% zirconium *n*-propoxide to 30 wt%. The solution pH is adjusted to 9 by ammonia. Glucose and fructose are used as chelating agents and the prepared mixture is mixed with zirconium solution (1:4 mass ratio), and $LiMn_2O_4$ powders are added to the obtained sol. The gelation process is carried out at room temperature and during gelation process, ultrasonic stirrer is used with three different sonication power (table 1) for dispersion of $LiMn_2O_4$ particles inside the ZrO_2 sol. After the polymerization of ZrO_2 sol, the resulting gel is heated to 500°C for 5 h. The slurry of the attained powder is made by 10 wt% polyvinylidene fluoride (PVdF), 10 wt% carbon black, 80 wt% active material and then laminated on a 12 μm aluminium foil.

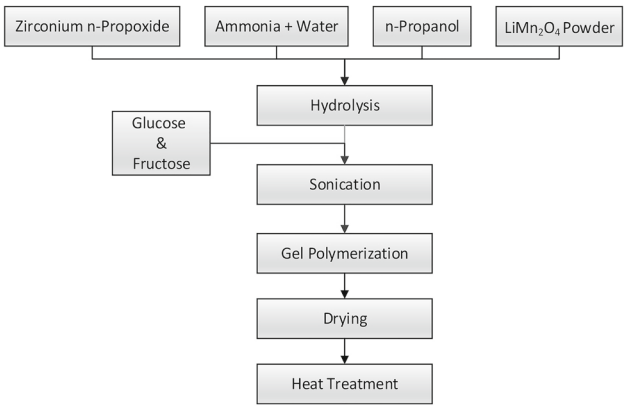

Figure 2. Synthesis procedure of ZrO_2-modified $LiMn_2O_4$ nanoparticles by sol–gel route.

2.2 *Materials characterization*

Morphological characterizations are analysed by a scanning electron microscope (SEM) (JEOL-JSM-5410LV). To

Table 1. ZrO_2 decoration parameters of $LiMn_2O_4$.

Sample code	Coating	ZrO_2 weight ratio (%)	Sonication power (%, Hz)	Sonication time (min)
Pure LMO	—	—	—	—
10%S-Zr@LMO	ZrO_2	5	10 (2 kHz)	60
30%S-Zr@LMO	ZrO_2	5	30 (6 kHz)	60
50%S-Zr@LMO	ZrO_2	5	50 (10 kHz)	60

observe the ZrO_2 distribution on $LiMn_2O_4$ surfaces, energy dispersive spectroscopy mapping (EDS) is carried out and the decoration ratio of ZrO_2 is calculated by J-Image program.

The structures of $LiMn_2O_4$ and ZrO_2 powders are analysed by Rigaku Miniflex XRD instrument. XRD analyses are performed at 2θ = 10°–80° with 2° min^{-1} scanning speed and Cu Kα radiation is used (λ = 1.54056 Å).

Surface areas of powders are measured with BET isotherm method in Micrometrics ASAP 2420. Samples are degassed at 200°C under 0.3–0.38 Pa for 3 h. After that, N_2 sorption is applied at 8 × 10^4 Pa.

2.3 *Electrochemical measurements*

To perform electrochemical tests, CR2032 half-cells are assembled and 1 M lithium hexafluorophosphate (BASF) in dimethyl carbonate:ethylene carbonate (7:3) by weight is selected as an electrolyte; a polypropylene film is used as a separator (Celgard).

Galvanostatic tests are carried out at room temperature (BST8-WA battery analyzer). C-rate tests are performed between 0.1 and 10C. Cyclic voltammetry (CV) and electrochemical impedance spectroscopy (EIS) analyses are performed at GAMRY Interface 1000E potentiostat. The EIS analyses are procured at 100 kHz to 1 MHz. The CV tests are measured between 3.0 and 4.5 V at a scan rate of 0.1 mV s^{-1}.

3. Results and discussion

The diffraction peaks of the LMO sample shown in figure 3 are in good agreement with PDF-No. 00-018-0736 and they correspond to the cubic spinel structure (space group Fd-3m). The spinel structure of $LiMn_2O_4$ contains 32 octahedral sites. Half of these sites are occupied by manganese ions and they can be found at Mn^{4+} and Mn^{3+} form. Therefore, each ion occupies 8 octahedral sites. While Mn^{4+} has a 0.54 Å ionic radius, the ionic radius of Mn^{3+} can change according to their spin state. For Mn^{3+} the ionic radius of low spin (LS) state is 0.58 Å, while the ionic radius of high spin (HS) state is 0.65 Å. Therefore, the difference between the ionic radius of Mn^{4+} and Mn^{3+} (LS) is only 0.04 Å; however, the difference between Mn^{4+} and Mn^{3+} (HS) is 0.11. Thus, an increase in the amount of HS Mn^{3+} leads higher lattice parameter (*a*) in LMO [29].

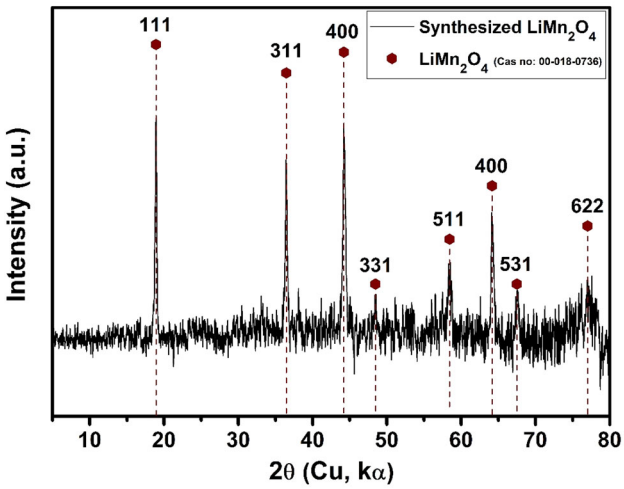

Figure 3. XRD pattern of synthesized $LiMn_2O_4$ powder.

The lattice parameter of PDF-No. 00-018-0736 and synthesized LMO is calculated as 8.242 Å ± 0.00207 and 8.2149 Å ± 0.00102, respectively. The reason for attaining lower *a* value is ascribed to a higher LS Mn^{3+} ratio. Chung *et al* [29] have asserted that temperature and time in heat treatment changes the valence state of Mn ions. They indicate that elevated calcination temperature causes valence transition from Mn^{4+} to Mn^{3+} (HS). In this study, it is observed that low calcination temperature (750°C) led to a higher Mn^{3+} (LS) ratio resulting in a lower lattice parameter.

Monoclinic and tetragonal crystal structures are determined in the XRD results (figure 4) of ZrO_2 powders. It is worth to note that at low temperatures, monoclinic-structured ZrO_2 is transformed into a semi-stable tetragonal phase due to the loss of OH^- ions in the amorphous $Zr(OH)_4$ gel above 400°C.

The scanning electron microscopy (SEM) analyses of pristine and ZrO_2-decorated LMO (figure 5) demonstrate that particle size varies between 500 and 1000 nm. In figure 5a, particles have sharp edges and smooth surfaces. However, after sonication treatment for 60 min, all coated particles had soft edges with rough surfaces. Moreover, as seen in figure 5b–d, particle size has reduced after

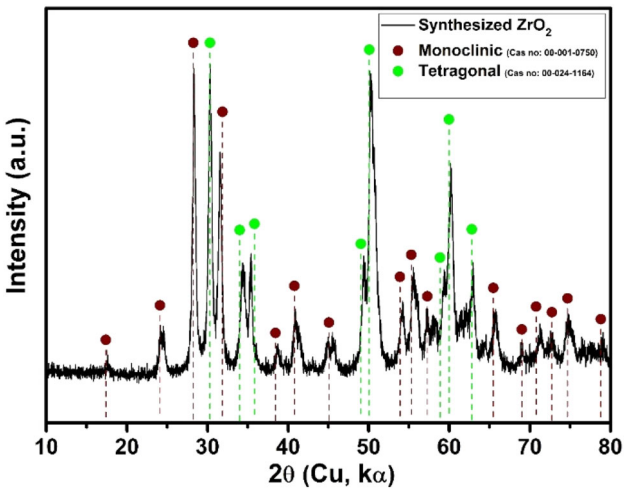

Figure 4. XRD pattern of synthesized ZrO_2 powder.

sonication treatment for all coated samples compared to the pure one. It is asserted that the LMO surfaces covered with ZrO_2 nano-sized particles resulting in rough surfaces, which are demonstrated with EDS mapping, as experienced by Wang *et al* [26]. Added to this, ultrasonic waves have made an effect on the particle size and shape. SEM images show that ultrasonication is particularly effective in reducing the particle size. Similar results have been reported for different metal oxides ($LiNi_{0.6}Co_{0.2}Mn_{0.2}O_2$, $LiCoO_2$, $LiFePO_4$) [30–32].

Specific surface area (SSA) results of pure and ZrO_2-decorated LMOs also support our assumptions about particle size reduction due to the sonication (table 2). The highest surface area is achieved at 50% sonication power with 7.47 $m^2\ g^{-1}$ and it is nearly 30% higher than pure LMO. As ultra-fine particles have high surface energy, they can quickly agglomerate by the strong adhesive force among them and that leads to relatively larger bodies with weak joining interfaces. Therefore, this difference among SSAs indicates that ascending sonication power can lead to a deagglomeration of those primary particles by damaging Van der Waals and Coulomb forces [33].

The EDS mapping results of the laminated electrodes for all sonication powers are given in figure 6. Mn atoms of LMO and Zr atoms of ZrO_2 are spotted in the same region, indicating that ZrO_2 decorated uniformly on the surface of LMO. With this decoration, direct contact between the cathode active material and the electrolyte reduced, which

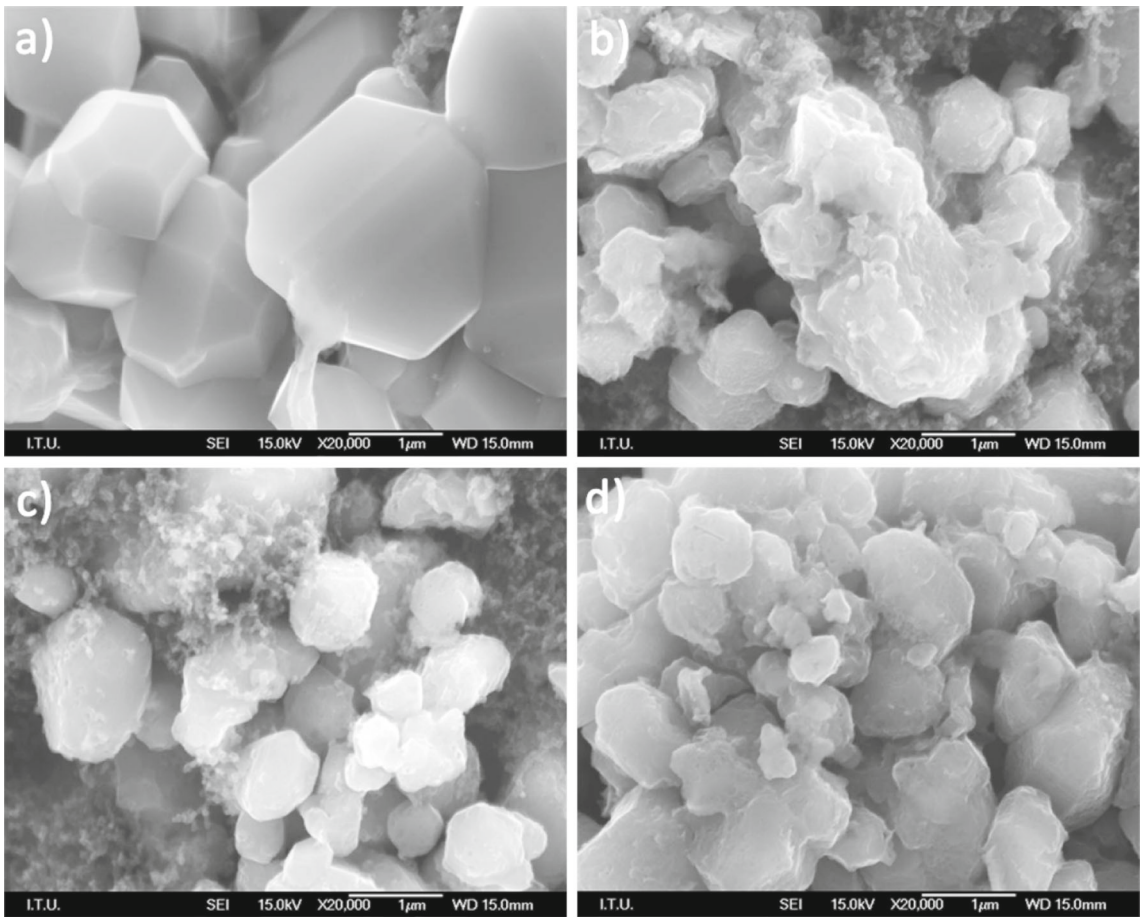

Figure 5. SEM images of (**a**) pure LMO, (**b**) 10%S-Zr@LMO, (**c**) 30%S-Zr@LMO and (**d**) 50%S-Zr@LMO.

will decrease the decomposition of electrolyte at elevated voltages during cycling and result in improved cyclic performance. In order to compare the decoration (distribution) ratio of different sonication powers, J-image program is used to analyse samples that are decorated with ZrO_2. SEM images with 10k magnification from each sample are chosen for this method. As seen in table 3, Zr ratio is slightly increased with the ascending sonication power and 20.38% is obtained at 50%S-Zr@LMO.

Table 2. Specific surface area of pure and ZrO_2-decorated $LiMn_2O_4$ samples.

Sample code	Surface area (m^2 g^{-1})
Pure	5.78
10%S-Zr@LMO	6.26
30%S-Zr@LMO	6.63
50%S-Zr@LMO	7.47

The first discharge capacity of pristine, 10%S-Zr@LMO, 30%S-Zr@LMO and 50%S-Zr@LMO electrodes at 0.1C are 124.2, 125.9, 126.1, 127.1 mAh g^{-1} and their capacity retentions at 100^{th} cycle are 53.2, 67.9, 70.6 and 73.4 mAh g^{-1}, respectively (figure 7). Although pure LMO shows a good first discharge capacity, it suffers fast fading. The reason for this capacity fade, which is also one of the main drawbacks for spinel $LiMn_2O_4$, is the dissolution of

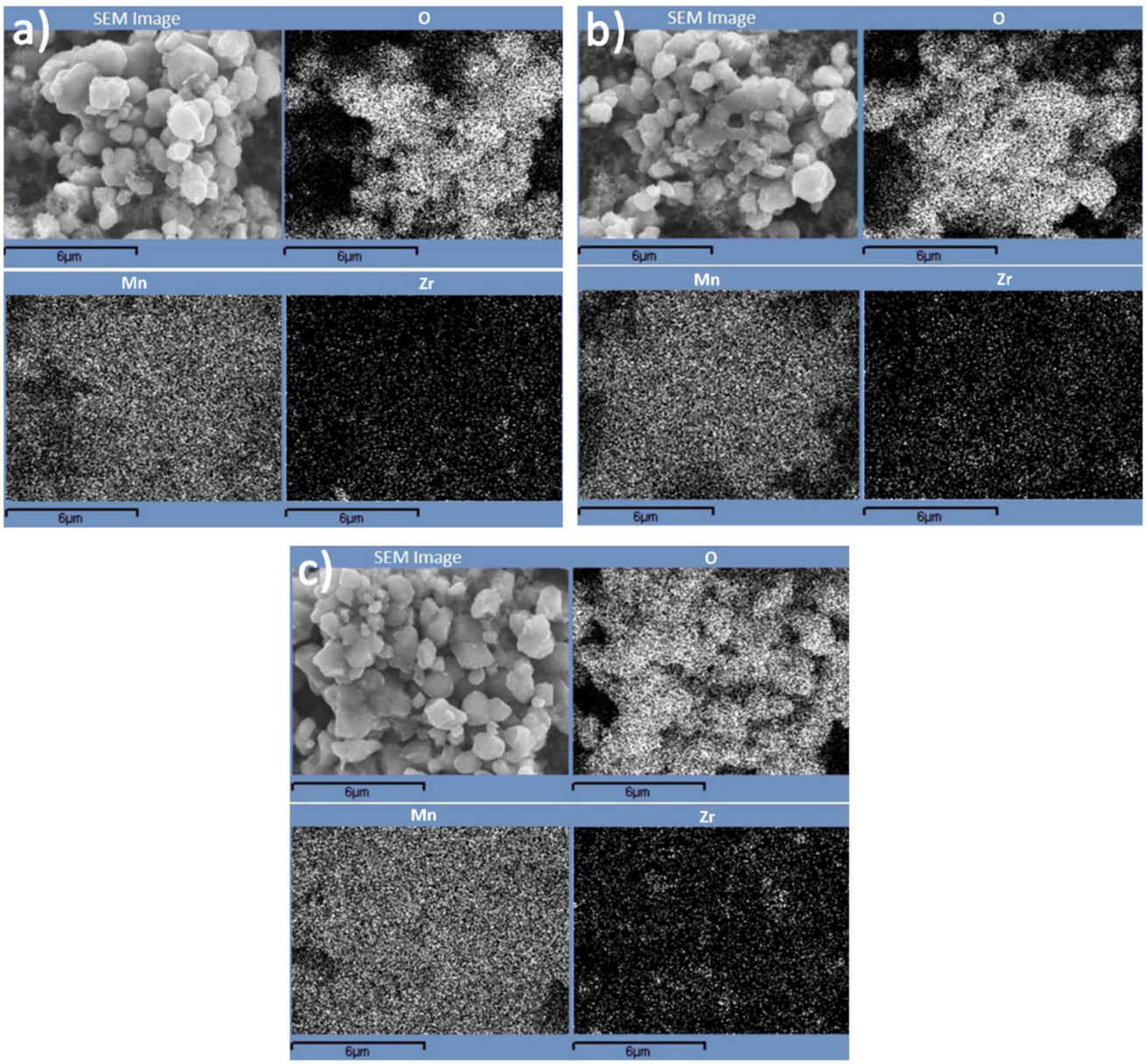

Figure 6. EDS mapping of (**a**) 10%S-Zr@LMO, (**b**) 30%S-Zr@LMO and (**c**) 50%S-Zr@LMO.

Table 3. Distribution ratio of Zr ions over $LiMn_2O_4$ particles via J-image program.

Sample code	ZrO_2 distribution ratio (%)
10%S-Zr@LMO	18.6
30%S-Zr@LMO	19.24
50%S-Zr@LMO	20.38

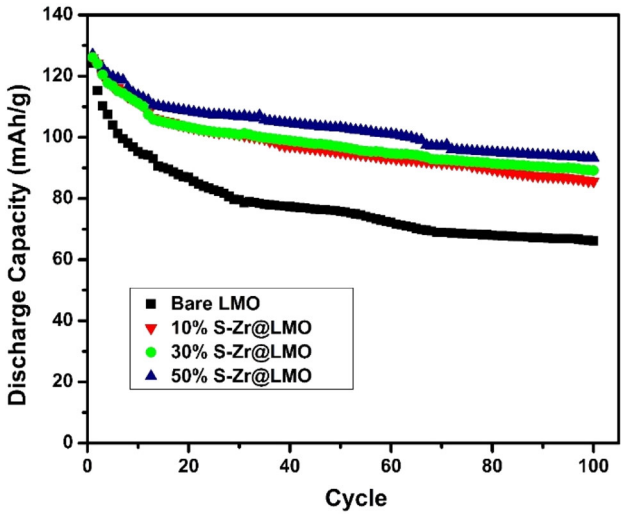

Figure 7. Cycling performance of pure LMO, 10%S-Zr@LMO, 30%S-Zr@LMO and 50%S-Zr@LMO at 0.1C in the voltage range of 3.0–4.5 V at room temperature (20°C).

Mn^{2+} ions in the presence of HF that occurred from $LiPF_6$-based electrolyte. This leads to rapid capacity loss during cycling. The reactions for Mn dissolution are given in equations (1–3) [34,35].

$$LiPF_6 \rightarrow PF_5 + LiF \quad (1)$$

$$PF_5 + H_2O \rightarrow PF_3O + 2HF \quad (2)$$

$$2LiMn_2O_4 + 4H^+ \rightarrow 3MnO_2 + Mn^{2+} + 2Li^+ + 2H_2O \quad (3)$$

As has been pointed out in table 4, the discharge capacity of all ZrO_2-modified electrodes demonstrated better capacity retention than the pristine sample. This clearly shows that the abovementioned reactions are suppressed and better cycling stability is attained with surface decoration, which will be further supported by the following CV results.

As for ZrO_2-modified LMOs with different sonication powers, though the first discharge capacities are similar, their capacity retentions at the 100th cycle slightly increase with the ascending sonication power. Among all decorations, 5 wt% ZrO_2-decorated electrode with 50% sonication power (10 kHz) shows the highest cycling retention. It is also important to mention that the sonication-assisted method provides slightly better performance than the magnetic stirring assisted method. Lim and Cho [36] synthesized PVP-assisted ZrO_2-coated $LiMn_2O_4$ by using magnetic stirring during the coating procedure. Attained discharge capacity is 2–3% lower than 50%S-Zr@LMO at the 50th cycle. On the other hand, the cyclic performance of ball milling assisted coating methods showed much better cycling performance than sonicated routes. Li *et al* [37] synthesized ZrO_2-coated $LiMn_2O_4$ via sintering process. In order to obtain a homogenous coating, ball milling is used to spread ZrO_2 over $LiMn_2O_4$ particles. Specific discharge capacity obtained at the end of 100 cycles from Li *et al*'s sample is 6% higher than our 50%S-Zr@LMO, which indicates better ZrO_2 distribution attained via ball milling.

In figure 8, the CV profile of the pure LMO is compared with ZrO_2-modified LMOs in the first 4 cycles. Three noticeable features can be seen in the CV plots. First, all decorated LMOs show smaller reduction/oxidation potential intervals than pure LMO that indicates a decrease in polarization after ZrO_2 modification. Second, all reduction and oxidation peaks in the ZrO_2-decorated samples are sharper than pure LMO, implying a fast electrode reaction after ZrO_2 decoration. The previous two statements demonstrate that ZrO_2 surface modification can enhance the kinetic properties of $LiMn_2O_4$. In pure LMO, two pairs of separated and well-defined redox peaks can be clearly observed, indicating that lithium ion intercalation/de-intercalation into/from $LiMn_2O_4$ [38,39]. This indicates that LMO undergoes two phases of reversible reduction and oxidation processes, which are $LiMn_2O_4/Li_{0.5}Mn_2O_4$ and $Li_{0.5}Mn_2O_4/\lambda$-MnO_2 [40].

$$LiMn_2O_4 \leftrightarrow Li_{1-x}Mn_2O_4 + x0.5Li^+ + x0.5e^- \ (x < 0.5)$$

Table 4. Electrochemical performance of pure and ZrO_2-decorated $LiMn_2O_4$ samples.

Sample code	Initial discharge capacity (mAh g^{-1}) at 0.1C	Capacity after 100 cycle (mAh g^{-1}) at 0.1C	Retention (%)
Pure	124.24	66.13	53.2
10%S-Zr@LMO	125.95	85.61	67.9
30%S-Zr@LMO	126.17	89.15	70.6
50%S-Zr@LMO	127.05	93.26	73.4

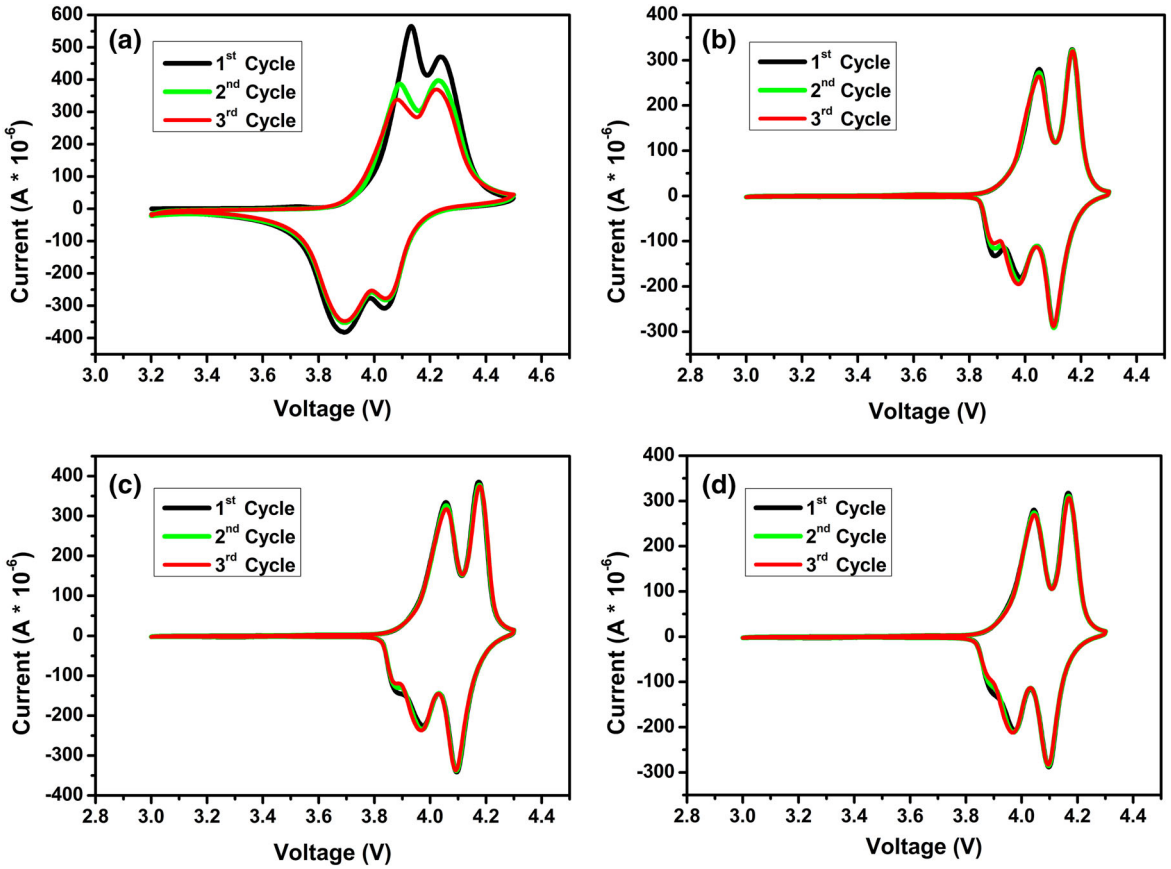

Figure 8. Cyclic voltammograms of (**a**) pristine, (**b**) 10%S-Zr@LMO, (**c**) 30%S-Zr@LMO and (**d**) 50%S-Zr@LMO in the voltage range of 3.0–4.5 V at room temperature.

$$Li_{1-x}Mn_2O_4 \leftrightarrow 2MnO_2 + (1-x)Li^+ + (1-x)5e^- \ (x > 0.5)$$

Lithium ions are extracted and inserted from/into half of the 8a tetrahedral at 4.13/3.09 V (*vs.* Li/Li^+), where lithium ions have the nearest-neighbour Li–Li interactions. The remaining lithium ions are extracted and inserted from/into other 8a tetrahedral sites at 4.23/4.04 V (*vs.* Li/Li^+), where Li–Li interactions do not take place [38]. Lastly, in decorated samples, three different peaks are obtained instead of two during the discharge process, where lithium intercalated into $Li_{0.5}Mn_2O_4$. In the pristine sample, anodic peaks are at 3.89 and 4.04 V (*vs.* Li/Li^+), but in the decorated samples, these peaks are shifted to 3.96 and 4.09 V (*vs.* Li/Li^+) due to the polarization. Moreover, the peak at 3.89 V can still be seen in all decorated samples. This indicates that a homogenous film formation could not be achieved and still uncoated regions remained after the decoration process. EDS mapping results and the Zr decoration ratios obtained from J-image calculations also support that there are still undecorated regions. Therefore, the insertion of lithium ions into $Li_{0.5}Mn_2O_4$ during the charging process might occur in two phases, where lithium ions are inserted from coated regions and uncoated regions with different voltages. In addition to that, despite the peak at 3.89 V is slightly stronger than the peak at 4.04 V, this situation is changed to the opposite in all ZrO_2-decorated samples and the peak at 3.89 V became less prominent. Because of the intercalation of lithium ions into $Li_{0.5}Mn_2O_4$ during the charging process proceeded in two phases, one strong peak that should be at 3.96 divided into two (3.89 and 3.96 V *vs.* Li/Li^+). However, with ascending sonication power, the peak at 3.89 V started to fade due to the increase in decorated regions (figure 8b–d).

To understand the diversity in capacity retention between the pure and decorated cathodes, EIS analyses are carried out after first, third and twentieth cycles at 3.0 V over a frequency range from 1 MHz to 100 kHz. Nyquist plots of the samples are given in figure 9a–e. The shift of impedance at Z_0 axis signifies the solution resistance (Rs). The semicircle at high frequency region is attributed to resistance of the surface, including SEI and ZrO_2 decoration (Rsf) [41]. The slope in low frequency regions is related to charge transfer resistance (Rct) and the solid-state diffusion of lithium-ion in the active material [42]. In figure 9f, the equivalent circuit that fits with all the plots is

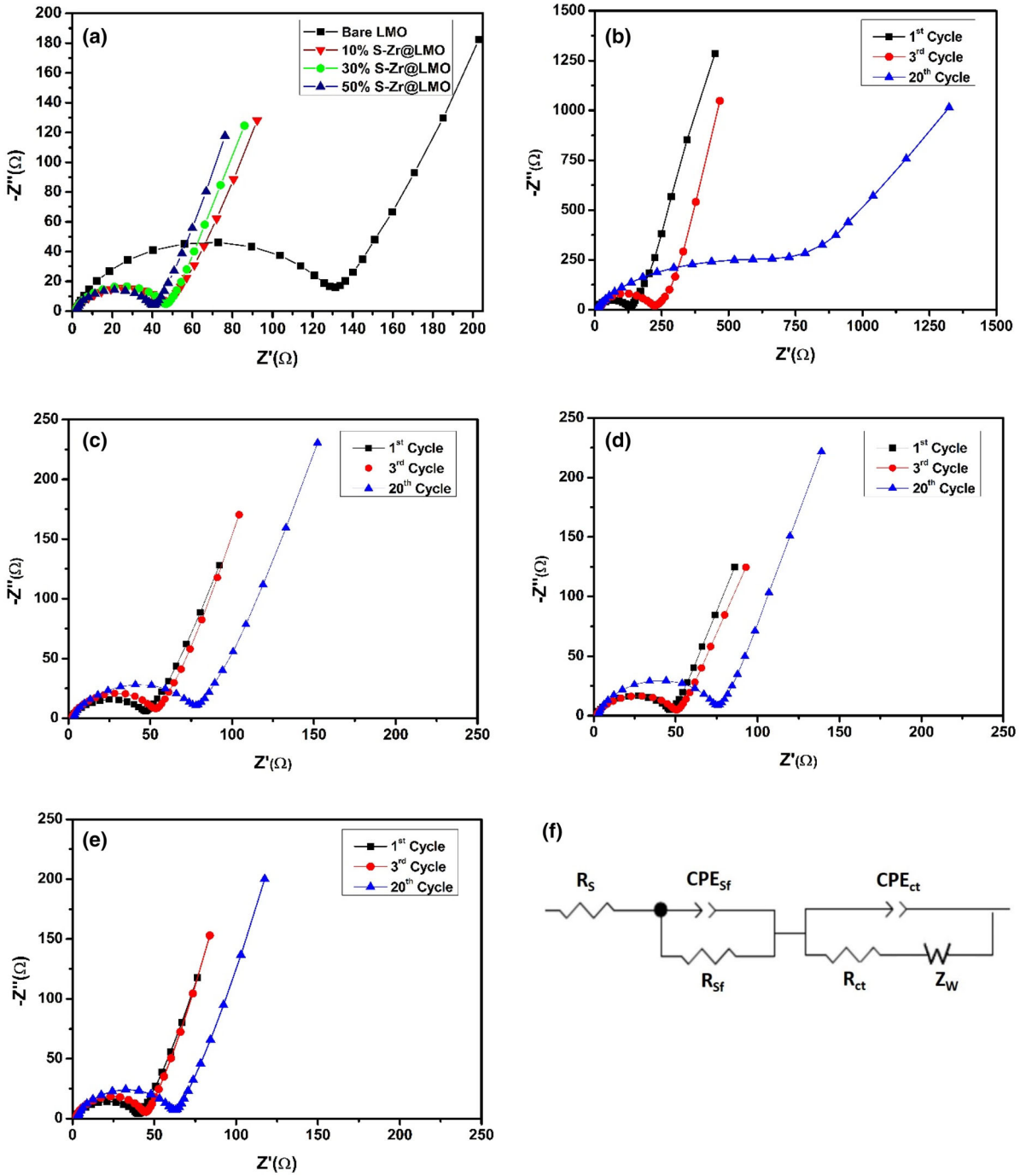

Figure 9. (**a**) Nyquist plots of pure and ZrO_2-decorated $LiMn_2O_4$ electrodes after 1st cycle at 3.0 V. Nyquist plots of (**b**) pure, (**c**) 10%S-Zr@LMO, (**d**) 30%S-Zr@LMO and (**e**) 50%S-Zr@LMO cells at 3.0 V with number of cycles; first, third and twentieth cycle and (**f**) their corresponding equivalent circuit.

demonstrated and the parameters determined from related equivalent circuit are given in table 5. The first cycle results showed that ZrO_2-decorated LMO samples have considerably smaller surface resistance (Rsf) than the pure LMO and the charge transfer resistance (Rct) decreased with ascending sonication power by obtaining more uniform ZrO_2 decoration. However, in different studies slightly larger Rsf is attained if the coating material ratio is 5 wt% or higher due to the low conductivity of ZrO_2 [43,44]. In our situation, polarization caused by ZrO_2 decoration is surpassed as the LMO particles exposed ultrasonic waves during the decoration process, which

Table 5. Rs, Rsf and Rct calculation of the samples at 1st, 3rd and 20th cycle on an equivalent circuit of the cell.

	1st Cycle (Ω cm^2)			3rd Cycle (Ω cm^2)			20th Cycle (Ω cm^2)		
Sample code	Rs	Rsf	Rct	Rs	Rsf	Rct	Rs	Rsf	Rct
Pure	3.34	253.8	152.2	3.68	591.1	343.62	6.18	1147.68	1498.71
10%S-Zr@LMO	2.98	90.6	93.98	3.33	100.42	108.65	5.62	147.9	156.31
30%S-Zr@LMO	2.95	88.98	83	3.29	96.12	89.48	5.33	144.2	133.88
50%S-Zr@LMO	3.43	75.56	76.98	3.77	83.91	83.88	5.19	120.36	114.54

leads to higher SSA for the decorated samples as shown in BET results. Thus, higher lithium migration through particle surface and lower Rsf value are obtained due to the increase of the contact area between electrolyte and cathode active material.

As listed in table 5, after 20 cycles ZrO_2-decorated samples demonstrated small changes in the Rsf, while pure LMO showed a significant rise in Rsf (see figure 9b). These results indicate that ZrO_2 decoration could reduce the contact between the electrolyte and electrode and alleviating the growth of undesired SEI film, which leads to a more stable interface during cycling. Furthermore, it can be found that the Rct of the pure LMO after 20 cycles is much higher than that of all the decorated samples, resulting in a higher diffusion of lithium ions in electrode. The attained results indicate that the ZrO_2 decoration can considerably facilitate the kinetics of Li diffusion during the cycling process.

The effects of the above-mentioned impedance results can be seen directly in the C-rate tests (figure 10). The data reveal that all decorated samples deliver better discharge capacities compared to pure LMO at high C rates, demonstrating that ZrO_2 decoration successfully enhances the rate performance of LMO. And, among the all decorated electrodes 50%S-Zr@LMO shows slightly better rate performance. Moreover, the discharge capacity totally restored after the C-rate is set to 0.2C, indicating that ZrO_2-modified LMO electrode has improved structural stability and electrochemical reversibility than pure LMO. 50%S-Zr@LMO sample also demonstrates ~7% higher specific discharge capacity at 2C rate when compared with study of Walz *et al*'s [45] magnetic stirring assisted ZrO_2-coated $LiMn_2O_4$. Even though they used a similar sol–gel route like in our study, magnetic stirring might not able to distribute zirconium n-propoxide over $LiMn_2O_4$ at a viscous environment as effectively as sonication.

In general, the reasons behind the capacity fading at spinel cathode are the corrosion reaction between the electrolyte and the cathode surface, and large lattice strain during charge–discharge process [46–48]. An atomistic simulation method has been accomplished by Benedek and Thackeray [49] for spinel $LiMn_2O_4$, which demonstrated that the {111} crystal faces contain

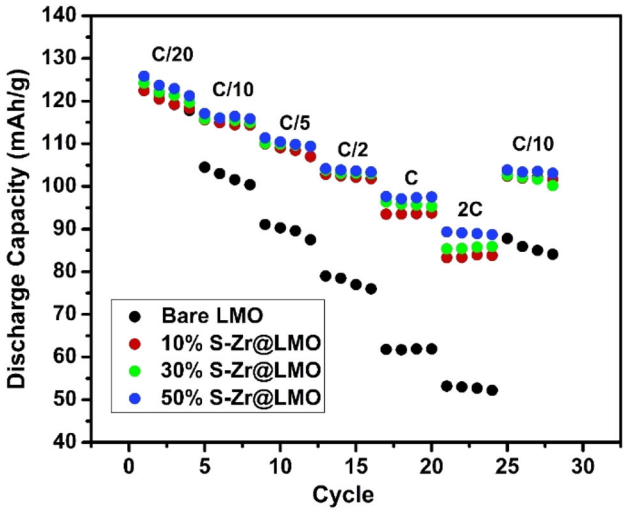

Figure 10. C-rate performance of pure LMO, 10%S-Zr@LMO, 30%S-Zr@LMO and 50%S-Zr@LMO in the voltage range of 3.0–4.5 V at room temperature (20°C).

the highest surface energy and suffer the most extensive rearrangements with electrolyte. If the Mn ions on the surface of (111) are mainly trivalent, it might hasten the surface corrosion due to the Jahn–Teller (J–T) distortion by Mn^{3+}. Therefore, cracks might occur at the edge of particles in spinel cathodes with proceeded cycles as experienced by Chen *et al*, but this effect might be minimized if higher Mn^{3+} (LS) is attained. The main reason for J–T distortion is having an odd number of electrons at e_g level in octahedral complexes. The distortion also happens if there is a degeneracy due to the electrons in the t_{2g} orbitals, but in the present structure higher Mn^{3+} (LS) is obtained due to low temperature heat treatment. As *d* orbital of Mn^{3+} ion has four electrons, the low spin state of d^4 complexes shows weaker J–T distortion compared to their high spin state [50,51]. SEM analyses after 100 cycles demonstrated that electrode morphology is well maintained and there are no cracks observed on the edge of LMO particles, which might indicate a weaker J–T distortion regarding the abovementioned issues (figure 11a–d).

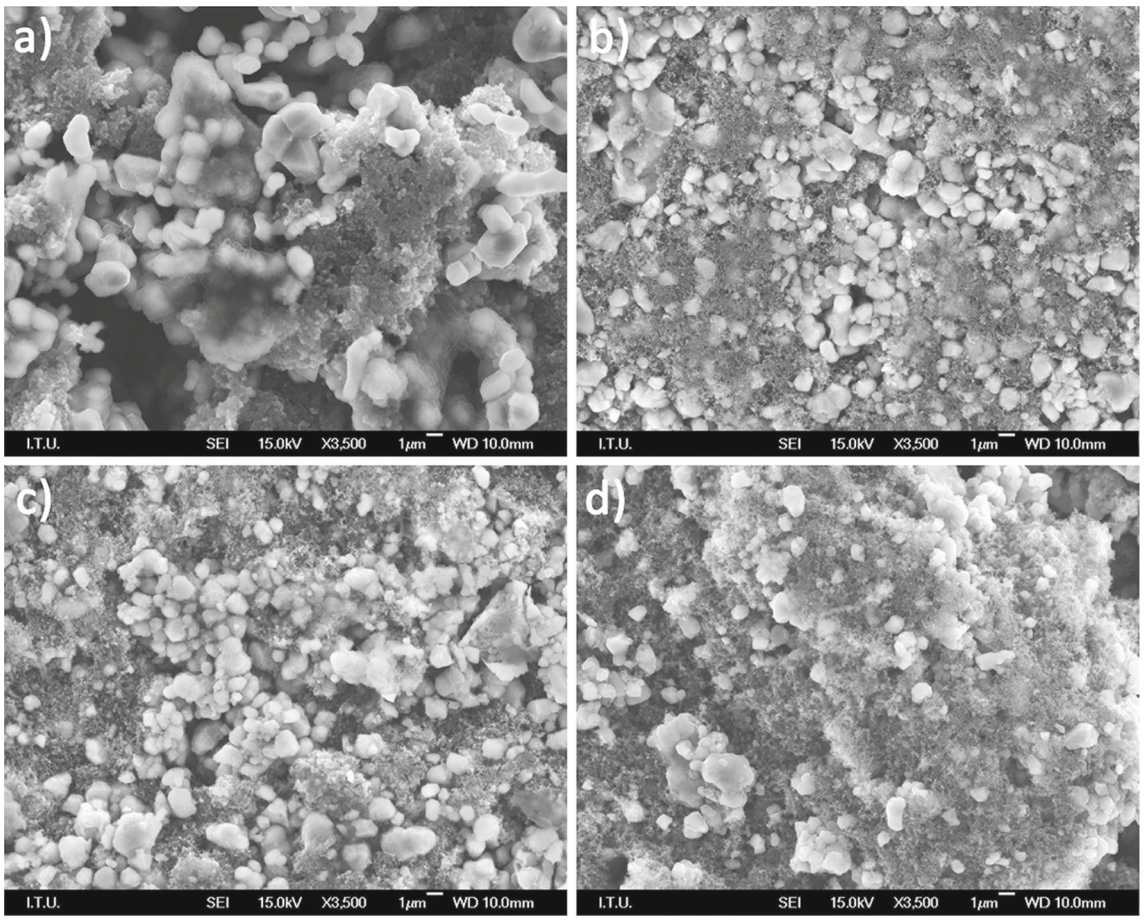

Figure 11. SEM images of (**a**) pure LMO, (**b**) 10%S-Zr@LMO, (**c**) 30%S-Zr@LMO and (**d**) 50%S-Zr@LMO after 100 cycles.

4. Conclusion

First, LMO powders are synthesized by sol–gel route. Then, ZrO_2 decoration on the powders with different sonication output powers is successfully applied via ultra-sonication-assisted sol–gel method. The ZrO_2 distribution on the LMO powders examined with J-image program using EDS mapping images. Uniform ZrO_2 distribution is attained with ascending sonication power. Electrochemical results indicated that the initial discharge capacity of the pure LMO electrode is 124.2 mAh g^{-1} and only 66.1 mAh g^{-1} could be retained (53.2% capacity retention) after 100 cycles. Comparatively, all the ZrO_2-decorated samples have shown better capacity retentions and rate performances. 50%S-Zr@LMO cathode (ZrO_2-decorated LMO with 50% sonication output power) demonstrates the best cycling performance compared with other sonication power levels at room temperature by 73.4% capacity retention and 93.2 mAh g^{-1} at 100 cycles.

Acknowledgements

We thank Prof. Dr Gultekin Goller and Huseyin Sezer for their aids to attain XRD and SEM characterizations. We also thank Istanbul Technical University Scientific Research Projects Department for their supports about this study (Project ID: BAP 39312).

References

[1] Tarascon J M and Armand M 2001 *Nature* **414** 359
[2] Wagnera R, Krafta V, Streiperta B, Kasnatscheewa J, Gallusa D R, Amerellera M *et al* 2017 *Electrochim. Acta* **228** 9
[3] Li L, Yao Q, Zhu H, Chen Z, Song L and Duanet J 2009 *Int. J. Refract. Metals Hard Mater.* **27** 78
[4] Uygur C S, Piskin B and Aydinol M K 2019 *Bull. Mater. Sci.* **42** 205
[5] Gao K, Zhao S X, Guo S T and Nan C W 2016 *Electrochim. Acta* **206** 1

[6] Olszewska D and Rutkowska A 2018 *Bull. Mater. Sci.* **41** 16
[7] Dixit M, Markovsky B, Aurbach D and Majorz D T 2017 *J. Electrochem. Soc.* **164** A6359
[8] Kim D K, Muralldharan P, Lee H W, Ruffo R, Yang Y, Chan C K *et al* 2008 *Nano Lett.* **8** 3948
[9] Bhandari A and Bhattacharya J 2017 *J. Electrochem. Soc.* **64** A106
[10] Taniguchi I, Song D and Wakihara M 2002 *J. Power Sources* **109** 333
[11] Aurbach D, Markovsky B, Talyossef Y, Salitra G, Kim H J and Choi S 2006 *J. Power Sources* **162** 780
[12] Fang X, Ge M, Rong J and Zhou C 2013 *J. Mater. Chem. A* **1** 4083
[13] Lim S and Cho J 2008 *Chem. Commun.* **37** 4472
[14] Liu D, Liu X and He Z 2007 *J. Alloys Compd.* **436** 387
[15] Dedryvère R, Laruelle S, Grugeon S, Gireaud L, Tarascon J M and Gonbeauet D 2005 *J. Electrochem. Soc.* **152** A689
[16] Jo C H, Cho D H, Noh H J, Yashiro H, Sun Y K and Myunget S T 2015 *Nano Res.* **8** 1464
[17] Zhou A, Wang W, Liu Q, Wang Y, Yao X, Qing F *et al* 2017 *J. Power Sources* **362** 131
[18] Schipper F, Bouzaglo H, Dixit M, Erickson E M, Weigel T, Talianker M *et al* 2018 *Adv. Energy Mater.* **8** 1701682
[19] Zhu X, Wang Y, Shang K, He W, Ai X, Yang H *et al* 2015 *J. Mater. Chem.* **3** 17113
[20] Lee S H, Yoon C S, Amine K and Sun Y K 2013 *J. Power Sources* **234** 201
[21] Gan Q, Qin N, Zhu Y, Huang Z, Zhang F, Gu S *et al* 2019 *ACS Appl. Mater. Interfaces* **11** 12594
[22] Han H, Qiu F, Liu Z and Han X 2015 *Ceram. Int.* **41** 8779
[23] Wua H M, Belharouaka I, Abouimranea A, Sunb Y K and Amine K 2010 *J. Power Sources* **195** 2909
[24] Zhao J and Wang Y 2013 *Nano Energy* **2** 882
[25] Lin Y M, Wu H C, Yen Y C, Guo Z Z, Yang M H, Chen H M *et al* 2005 *J. Electrochem. Soc.* **152** A1536
[26] Wang Z, Liu E, Guo L, Shi C, He C, Li J *et al* 2013 *Surf. Coat. Technol.* **235** 570
[27] Machida N, Kashiwagi J, Naito M and Shigematsu T 2012 *Solid State Ion.* **225** 354
[28] Chung K Y, Yoon W S, Lee H S, McBreen J, Yang X Q, Oh S H *et al* 2006 *J. Power Sources* **163** 185
[29] Chung H T, Myung S T, Cho T H and Son J T 2001 *J. Power Sources* **97–98** 454
[30] Chen Y, Zhang Y, Wang F, Wang Z and Zhang Q 2014 *J. Alloys Compd.* **611** 135
[31] Zhao S, Zhang W, Li G, Zhu H, Huang J and He W 2020 *J. Cleaner Product.* **257** 120510
[32] Hu G, Xie X, Cao Y, Xu L, Du K, Wang W *et al* 2019 *J. Alloys Compd.* **773** 1165
[33] Rajabzadeh G, Salehi S and Jalalian A 2010 *Synth. React. Inorg. Metal Org. Nano-Metal Chem.* **40** 922
[34] Aurbach D 2000 *J. Power Sources* **89** 206
[35] Tu J, Zhao X B, Cao G S, Tu J P and Zhuet T J 2006 *Mater. Lett.* **60** 3251
[36] Lim S H and Cho J 2008 *Electrochem. Commun.* **10** 1478
[37] Li G, Chen X, Liu Y, Chen Y and Yang W 2018 *RSC Adv.* **8** 16753
[38] Xia Y and Yoshio M 1996 *J. Electrochem. Soc.* **143** 825
[39] Ott A, Endres P, Klein V, Fuchs B, Jager A, Mayer H A *et al* 1998 *J. Power Sources* **72** 1
[40] Thackeray M M, David W I F, Bruce P G and Goodenough J B 1983 *Mater. Res. Bull.* **18** 461
[41] Bai Y, Yin Y, Liu N, Guo B, Shi H, Liu J *et al* 2007 *J Power Sources* **174** 328
[42] Liu J and Manthiram A 2009 *J. Phys. Chem. C* **113** 15073
[43] Kim W-K, Han D-W, Ryu W-H, Lim S-J and Kwon H-S 2012 *Electrochim. Acta* **71** 17
[44] Akbulut A, Cetinkaya T, Guler M O and Akbulut H 2014 *Acta Phys. Polonica A* **125** 331
[45] Walz K A, Johnson C S, Genthe J, Stoiber L C, Zeltner W A, Anderson M A *et al* 2010 *J. Power Sources* **195** 4943
[46] Hai B, Shukla A K, Duncan H and Chen G Y 2013 *J. Mater. Chem. A* **1** 759
[47] Mukerjee S, Yang X Q, Sun X, Lee S J, McBreen J and Ein-Eli Y 2004 *Electrochim. Acta* **49** 3373
[48] Amatucci G and Tarascon J M 2005 *J. Electrochem. Soc.* **149** K31
[49] Benedek R and Thackeray M M 2011 *Phys. Rev. B* **83** 195439
[50] Jahn H A and Teller E 1967 *Proc. Royal Soc. A* **161** 220
[51] Onishi T 2012 in *Advances in quantum chemistry* J S E Brandas (ed) (New York: Academic Press) p 31